Snapshots from Cryo-ET of active SARS-CoV-2 virions

Hideo Fukuhara[1,2,3,#], Hisham M. Dokainish[2,#,*], Shunsuke Kita[2], Koshiro Tabata[4,5], Akira Takasu[6], Juha T. Huiskonen[7], Yuki Anraku[2], Toshiya Senda[6,8,9], David I. Stuart[10], Michihito Sasaki[4], Yasuko Orba[4], Yasuhiko Suzuki[5,11,*], Hirofumi Sawa[4,5,12,13,*] & Katsumi Maenaka[1,2,3,5,12,14,*].

[1] Division of Pathogen Structure, International Institute for Zoonosis Control, Hokkaido University, Kita-20, Nishi-10, Kita-ku, Sapporo 001-0020, Japan.

[2] Laboratory of Biomolecular Science and Center for Research and Education on Drug Discovery, Faculty of Pharmaceutical Sciences, Hokkaido University, Kita-12, Nishi-6, Kita-ku, Sapporo 060-0812, Japan.

[3] Global Station for Biosurfaces and Drug Discovery, Hokkaido University, Kita-12, Nishi-6, Kita-ku, Sapporo 060-0812, Japan

[4] Division of Molecular Pathobiology, International Institute for Zoonosis Control, Hokkaido University, Kita-20, Nishi-10, Kita-ku, Sapporo 001-0020, Japan

[5] Institute for Vaccine Research and Development (HU-IVReD), Hokkaido University, Kita-21, Nishi-11, Kita-ku, Sapporo 001-0020, Japan

[6] Structural Biology Research Center, Institute of Materials Structure Science, High Energy Accelerator Research Organization (KEK), Tokyo 135-0063, Japan

[7] Institute of Biotechnology, Helsinki Institute of Life Science HiLIFE, University of Helsinki, P.O. Box 56, 00014 Helsinki, Finland.

23 [8] Department of Accelerator Science, School of High Energy Accelerator Science, SOKENDAI
24 (the Graduate University for Advanced Studies), 1-1 Oho, Tsukuba, Ibaraki 305-0801, Japan
25 [9] Faculty of Pure and Applied Sciences, University of Tsukuba, 1-1-1 Tennodai, Tsukuba, Ibaraki
26 305-8572, Japan
27 [10] Division of Structural Biology, University of Oxford, The Wellcome Centre for Human Genetics,
28 Headington, Oxford OX3 7BN, UK; Chinese Academy of Medical Sciences Oxford Institute,
29 University of Oxford, Oxford OX3 7FZ, UK; Diamond Light Source Ltd, Harwell Science &
30 Innovation Campus, Didcot OX11 0DE, UK; Nuffield Department of Medicine, Wellcome Centre
31 for Human Genetics, University of Oxford, Oxford OX3 7BN, UK.
32 [11] Division of Bioresources, International Institute for Zoonosis Control, Hokkaido University,
33 Kita-20, Nishi-10, Kita-ku, Sapporo 001-0020, Japan
34 [12] One Health Research Center, Hokkaido University, Kita-19, Nishi-9, Kita-ku, Sapporo 001-
35 0020, Japan
36 [13] Global Virus Network, Baltimore, Maryland, USA
37 [14] Faculty of Pharmaceutical Sciences, Kyushu University, Fukuoka, 812-8582, Japan.
38
39 [#] Contributed equally.
40
41 *Correspondence authors:
42 Y.S. (email: suzuki@czc.hokudai.ac.jp)
43 H.D. (email: hisham.dokainish@pharm.hokudai.ac.jp)
44 H.S. (email: h-sawa@ivred.hokudai.ac.jp)
45 K.M. (email: maenaka@pharm.hokudai.ac.jp) (Lead Contact)

Abstract

Understanding the molecular properties of SARS-CoV-2 is crucial to tackle the continuing variant emergence as well as future outbreaks. Current structural knowledge of the trimeric spike protein is largely based on truncated recombinant proteins and inactivated full-length forms, which may suffer from overstabilization through designed mutations and chemical fixation. Here, we apply cryo-electron tomography (cryo-ET) at a Biosafety level 3 facility to study the virus structure in its native, active state. The virus particles show variable shapes with diffusible spikes. While the majority of spike proteins display typical prefusion trimer conformations, we identify atypical open-trimer prefusion states, revealing a hidden level of flexibility. The sub-tomogram averaged structure also suggests a loosely packed trimer structure. Spike dynamics reveal cryptic epitopes in conserved regions among coronaviruses that can be targeted for broadly effective vaccines. Therefore, the structural analysis of virus structures in their active forms will provide significant implications on fusion mechanism as well as vaccine and antibody/drug design.

60 **Main**

61 Severe acute respiratory syndrome coronavirus 2 (SARS-CoV-2) continues to impact global
62 health[1]. The ongoing emergence of new variants hinders the efficacy of developed vaccines and
63 therapeutic antibodies[2,3]. The spike protein decorates the virus surface and plays central roles in
64 the viral entry and immune shielding mechanisms[4,5]. The spike protein is a trimeric glycoprotein,
65 wherein each protomer is formed of two subunits (S1 and S2) with a transmembrane region[6].
66 Numerous studies elucidated spike protein structures and dynamics, paving the way for mRNA
67 vaccine developments[6-10]. Specifically, cryogenic electron microscopy (cryo-EM) has been used
68 to determine structures of the recombinant spike protein in wild-type and emerging variants[3,6-12].
69 Moreover, cryo-ET has enabled the study of full-length spikes in the inactivated viruses,
70 unraveling the flexibility of its stalk region and the protein distribution on the virus surface[7,13-18].
71 Structural studies provided fundamental information on the virus molecular structure, architecture,
72 interactions, and dynamics[4].

73 Despite the enormous amount of structural information available on SARS-CoV-2 virus and its
74 spike protein, our understanding of the virus in its active form is still lacking[19]. In fact, the majority
75 of cryo-EM studies are performed using a truncated ectodomain of the spike protein, which
76 includes several mutations (e.g. 2P and 6P proline mutations) designed to stabilize the prefusion
77 state[20,21]. Accordingly, several approved vaccines include similar proline mutations, for improving
78 production and stabilization[22]. Indeed, the proline mutations may induce local rigidity altering the
79 nearby secondary structure[23]. Likewise, to reduce biological hazards, chemical fixation is usually
80 applied in cryo-ET experiments[15,19]. Chemicals such as paraformaldehyde (PFA) are known to
81 interact with charged residues and may cause morphological changes that alter protein
82 structures[19,24]. In addition, electron (E)-beam inactivation was recently shown to be damaging to

83 spike protein structures[15]. According to previous structural studies, the spike protein has a
84 reasonably stable prefusion state with a number of conformational states that are governed by the
85 motion of its S1 receptor binding domains (RBDs) from Down to Up states[6]. In contrast, Hydrogen
86 Deuterium Exchange Mass Spectrometry (HDX-MS) study showed that the prefusion state of the
87 spike protein is quite dynamic, highlighting the existence of a form of the prefusion state in which
88 parts of S2 are exposed[23]. Furthermore, the binding of some antibodies to the S2 subunit in the
89 prefusion state suggests the formation of an unknown open trimer structure[25]. Collectively,
90 previous studies showed structural flexibility at several levels using artificially stabilized proteins
91 and inactivated viruses. However, true images of spike proteins are still missing.

92 Understanding the differences between the current structural knowledge of SARS-CoV-2 that
93 may suffer from overstabilization, and the active form is crucial for future vaccine and
94 antibody/drug development. Certainly, elucidating the dynamics of spike proteins in its native form
95 would shape the approach to targeting future variants. To address this point, we set up the high-
96 end cryo-electron microscope at a Biosafety level 3 (BSL3) area to employ cryo-ET and single-
97 particle tomography (SPT)[26] to unravel the structure of the spike protein using active viruses. In
98 this experiment, neither chemical fixation nor ultracentrifugation were applied, to avoid spike
99 structure alteration or detachment. To the best of our knowledge, this is the first structural study of
100 SARS-CoV-2 in its active form.

101

102 *BSL3 High-end Cryo-electron Microscope.*

103 We set up the latest generation of cryo-electron microscope (300 kV), Krios G4 (Thermo
104 Fisher Scientific) with a Falcon 4 direct electron detector and a Selectris energy filter in the
105 management area for BSL3 pathogens in the International Institute for Zoonosis Control,

106 Hokkaido University (**Fig. S1**). The detail of BSL3 cryo-EM system and procedure for handling
107 the grid preparation and data collection will be published elsewhere, but briefly, virus vitrification
108 using EM GP2 (Leica) and autogrid assembly were performed in the safety cabinet. The autogrid
109 was transferred to Krios G4 and cryo-ET data were collected (**Fig. S1**). This is one of the first
110 examples of operating a high-end cryo-electron microscope in the BSL3 area. The active SARS-
111 CoV-2 of the ancestral strain WK-521 in cell culture was directly frozen and observed. Thus, the
112 virus preparation did not include any ultracentrifugation or chemical fixation to avoid any kind of
113 artifacts as much as possible.
114
115 *The Pleomorphic Virus Particles Morphology.*
116 Early cryo-ET study of the inactivated SARS-CoV-2 demonstrated the formation of an
117 ellipsoidal or a spherical-shaped viral envelope, with an average of 96.6 nm for its longest axis[16].
118 In contrast, a more recent cryo-ET study suggested the formation of a dominant flat cylindrical
119 shape, in ancestral, alpha, beta and delta variants, with an average diameter of 102 nm[14]. Notably,
120 a later cryo-ET study of the delta variant has shown the formation of fused virus particles, where
121 one envelope encloses two sets of RNPs[15]. In summary, previous cryo-ET studies suggested some
122 level of pleomorphism.
123 In this study, 42 tomograms of the active ancestral virus were recorded and reconstructed,
124 including 46 virus particles **(e.g. Movie S1)**. A tilt angular step of 1°, covering a range from −60°
125 to +60° was used, resulting in 121 tilt images per tomogram. **Fig. 1** shows a variety of envelope
126 shapes, including dominant spherical (L1: 99 ± 13.6 nm, L2: 94 ± 13.6 nm) and ellipsoidal shapes
127 (L1: 117 ± 19.7 nm, L2: 94 ± 15.9 nm), as well as oval (L1: 99 ± 21.5 nm, L2: 87 ± 10.6 nm),
128 cylindrical (L1: 93 ± 7.9 nm, L2: 57 ± 10.1 nm) and bean-like (L1: 100 ± 12.7 nm, L2: 65 ± 10.9

nm) envelops (summarized in **Table S1**). The measured diameters of the two longest axes (L1 and L2) indicate a large variation in the virus size, wherein the maximum axis (L1) can vary from 72 to 150 nm (**Movie S2**). Remarkably, very large virus particles with L1:150, L2:125 (**Fig. 1c right**) and L1:139, L2:102 nm (**Fig. 1c left**) were observed. Such large particles may indicate the fusion of two virus particles in ancestral strain, as recently observed in delta variant[15]. **Fig. S2a and Movie S3** also show the observation of two virus particles apparently undergoing a fusion process. In addition, **Fig. S2b** suggests that there is no correlation between the observed morphology and ice thickness. It also shows that the third axis is correlated with the particle size. Collectively, unlike previous results from inactivated viruses that exhibit a dominant morphology, our results suggest a high level of flexibility, adaptability, and pleomorphism on virus shape in response to surrounding environments.

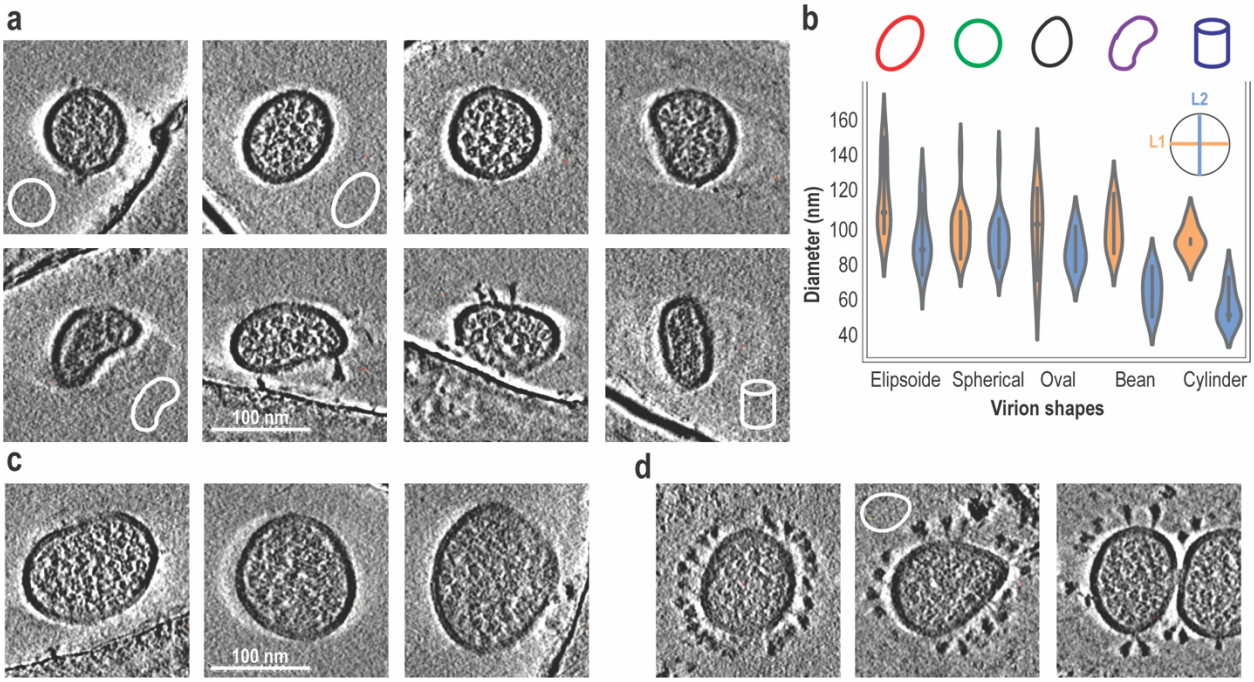

Figure 1. Pleomorphology of active virus particles. a) Central sections (7.5 nm thick) through the cryo-ET tomograms of the ancestral virions. b) Violin plot representation of the two longest diameters (L1 and

144 L2) in 46 virus particles. c) Tomograms slices of three virions with very large diameters (Left: L1:139,
145 L2:102; Middle: L1:125, L2:119; Right: L1:150, L2:125). d) Central slices of virions on carbon film.
146
147
148 *Spike Distribution and Arrangements.*
149 In the current dataset, one-third of the particles (14 out of 46) were observed on the carbon
150 film. These particles tend to include a higher density of spike proteins, in comparison to the ones
151 in the grid holes. On the carbon, spike proteins are pushed to the edge of the flattened particle,
152 reflecting high diffusibility within the native viral lipid membrane (**Fig. 1d**). Such high diffusibility
153 may allow the virus to relocate more spikes at the interface upon encountering natural host receptor,
154 Angiotensin-converting enzyme 2 (ACE2). On the other hand, within grid holes, spike proteins
155 are more dispersed on the surface, where fewer spikes can be identified in most cross sections. **Fig.**
156 **2a** shows that spike proteins can exist as a dimer of trimers or even a trimer of trimers (**Movie S1**
157 **right)**, and similar complexes were previously observed in full-length spike proteins from the
158 Novavax vaccine[27]. **Fig. S3** indicates the formation of two spike trimers with shared
159 transmembrane regions, as reported previously[16]. Such arrangements raise a question regarding
160 the possibility of protomer swapping between trimeric spike structures. Both 247 prefusion and 44
161 postfusion conformations were observed across active virus particles. Specifically, the postfusion
162 state was found to occur in clusters (**Fig. 2b**). Such arrangements of the postfusion state may
163 facilitate membrane fusion by attaching several fusion peptides at the same time.

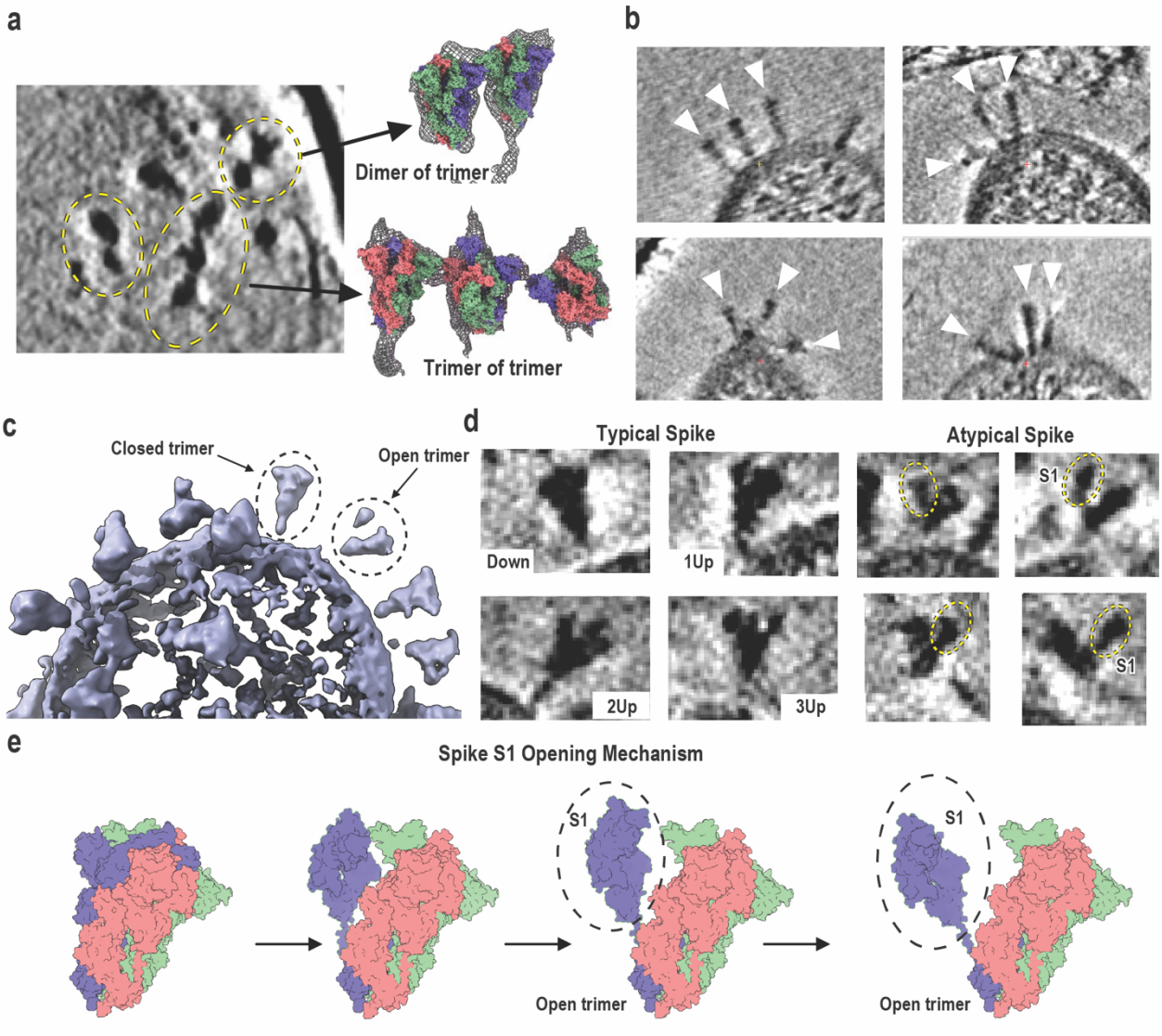

Figure 2. Distribution and atypical conformations of the spike protein. a) The 2D central slice of virus particle showing the formation of higher order structures including dimer of trimers and trimer of trimers. Isosurface is also shown in mesh representation, wherein PDB 6ZGE[10] is fitted and shown in surface representation. b) Tomograms slices (7.5 nm thick) of four virions with clusters of postfusion spike structures. Postfusion conformations are highlighted with white arrowheads. c) The isosurface representation of several spike proteins on the virus surface, wherein the closed/packed and open trimers of prefusion states can be identified as shown by dashed lines. d) The magnified view of 2D central slice tomograms of the typical spike protein densities including Down, 1Up, 2Up and 3Up conformations, as

173 well as atypical spike protein densities observed in active viruses. The detached S1 subunits are highlighted
174 by dashed lines. e) Proposed schematic representation of the spike opening mechanism at prefusion states,
175 in which one protomer S1 subunit undergoes a large conformational change.
176
177
178 *Atypical Spike Conformations Indicate an Open Trimer.*
179 **Fig. 2c and d** show all typical forms of the spike protein observed in our dataset. This
180 includes the prefusion Down, 1Up, 2Up and 3Up states, reflecting the inherent dynamical nature
181 of the spike protein, in the absence of ACE2 or neutralizing antibody (nAb). Notably, besides
182 typical conformations, atypical forms of the spike protein were also observed. Among these, spike
183 protomers may undergo large conformational changes, forming a novel open trimer state. Simple
184 fitting to a detached density indicates that the observed motion involves the S1 subunit of single
185 spike protomer. Accordingly, a range of open trimer structures can be seen (**Fig. 2d**), exposing the
186 S2 subunit. It is important to mention that most of spike protein conformations in our dataset were
187 typical prefusion states, where open trimer conformations occur in a small portion (~4%) of
188 observed prefusion states. These results suggest a hidden motion of the spike structure, in which
189 spike protomers are more flexible and can undergo conformational opening (**Fig. 2e)**. Consistently,
190 previous HDX-MS studies using the recombinant ectodomain of the spike protein with a prefusion
191 stabilization (2P mutations) suggested the minor presence of an alternative conformation, in which
192 S2 residues are solvent exposed, which can be targeted by nAbs, such as 3A3 and RAY53[22,23,25].
193 Therefore, in active viruses, the typical closed/packed prefusion conformation is dominant but the
194 spike protein itself has ability to spontaneously transit to an open-trimer conformation.

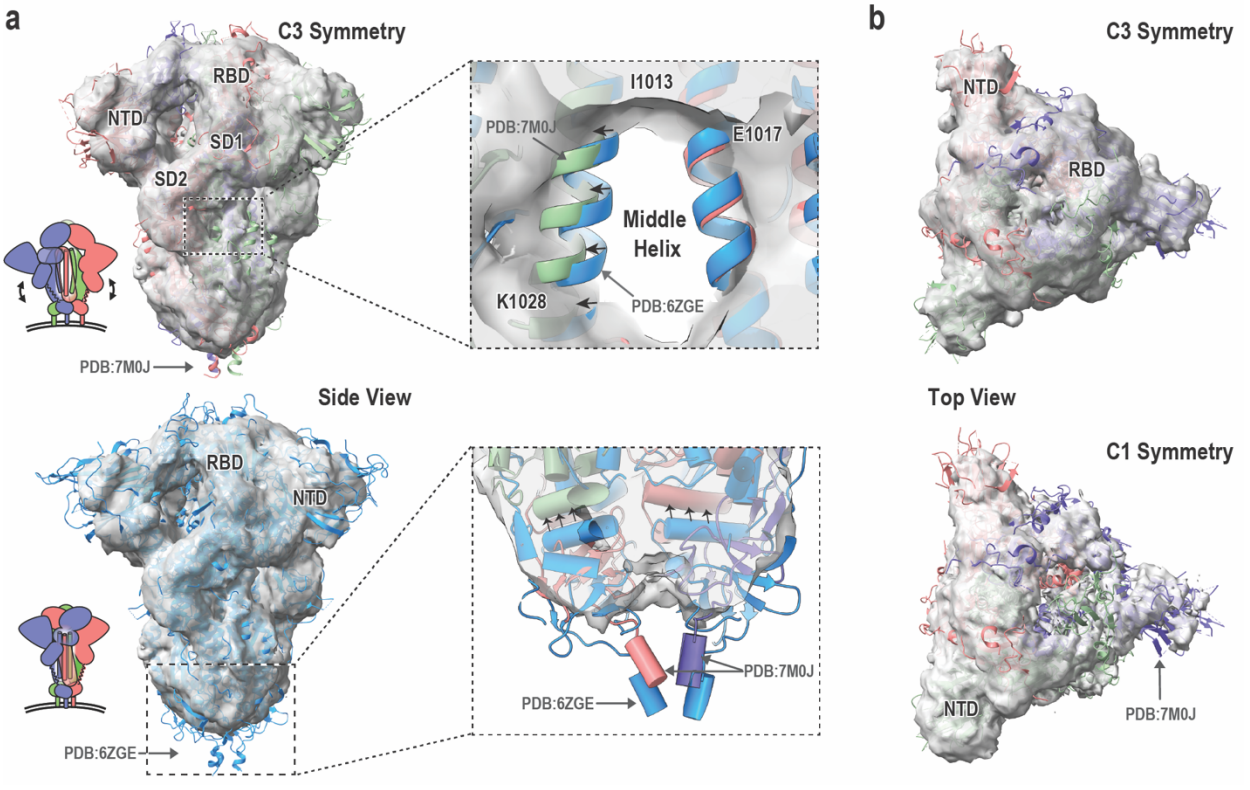

Figure 3. The spike protein averaged map obtained by SPT analysis. a) The sub-tomogram averaged map with the superimposition of cryo-EM structures of the spike trimer (PDB 7M0J; Top)) and (PDB 6ZGE; Bottom). Purple, green and pink colors were used to represent spike protomers. The zoomed-in view of the trimeric S2 interface from 7M0J (pink and green ribbons) and 6ZGE (blue ribbon), fitted into the spike protein average map (Top center), indicating the S2 variation in fitted middle helices. The zoomed-in view of the terminal part of spike protein averaged map (Bottom center) with fitted PDB structures, 7M0J (pink, green and purple ribbons) and 6ZGE (blue ribbon). Arrows in central panels indicate structural shifts from 6ZGE to 7M0J. b) Top views of the sub-tomogram averaged maps of the C3 symmetry (top) and the C1 symmetry (bottom) fitted with prefusion-state spike protein (PDB 7M0J).

209 *Spike Average Conformation Suggests a Loosely Packed Structure.*

210 To gain further insights into the mechanism of the open-trimer formation, we performed
211 single particle tomography (SPT) analysis of the prefusion packed conformation. 237 prefusion
212 spike particles were manually picked (excluding open trimer and postfusion states). Around 28,000
213 tilt images (121 tilt per particle) were used for the 3D re-construction, with a voxel size of 1.884
214 Å. To avoid any bias, no previously published maps of the spike protein were used in the alignment
215 and refinement processes. **Fig. 3a** and **Movie S4** show the sub-tomogram averaged map of the C3
216 symmetric spike protein, which was obtained with a global resolution of 14 Å (**Fig. S4**). In addition,
217 a C1 symmetry map was also obtained at a slightly lower global resolution of 17.0 Å, and this was
218 essentially similar to the C3 symmetric structure but with less density in one protomer (**Fig. 3b**).
219 The general features of the maps obtained are similar to those of previous Cryo-EM studies. A 2.6
220 Å resolution structure of the ancestral spike protein (PDB 6ZGE)[10] fits adequately in the obtained
221 low-resolution map (**Fig. 3a bottom**). However, a better fit was obtained using the asymmetrically
222 refined structure (PDB 7M0J) of the engineered spike (u1S2q) with quadruple mutations (A570L,
223 T572I, F855Y, N856I) [28,29] (**Fig. 3a top**), which was previously shown to exhibit intrinsic mobility,
224 evidenced by high propensity of forming 1Up and 2Up conformations and sustained binding to the
225 CR3022 antibody[29]. In detail, the SPT map shows missing density at the S2 middle helices
226 interface (**Fig. 3a top center**). The helices were elongated and contributed to forming tightly
227 packed S2 in many reported cryo-EM structures, however, there exists some variation of S2 middle
228 helices interface in cryo-EM structures. Our cryo-ET map fits better to the 7MOJ structure
229 harboring slightly bent helices (**Fig. 3a top center**). Notably, the S2 subunit shows multiple
230 regions with charged residues (**Fig. S5)** at the trimer interface and, in the 7MOJ structure, the S2
231 subunit makes hydrophobic interactions at the interface to avoid charge repulsion. In addition, **Fig.**

232 **3a bottom center** highlights the fitting of 6ZGE and 7M0J to the proximal part of the stem helices,
233 wherein the 7M0J structure shows an upward shift that again better fit the averaged map. Previous
234 principal component (PC) analysis of 165 protomers from 52 spike Down PDB structures, shows
235 a similar behavior where PC1 and PC2 modes both show up and down motion in S2 with respect
236 to S1, indicating structural variation within the available PDB structures[30]. Therefore, these
237 structural features allow for more flexible movement of the protomers and the formation of the
238 above-mentioned open trimer structure as well as the transition to postfusion (**Fig. 4**). Notably, a
239 recent sub-tomogram averaged map of Env protein (9.1 Å resolution) in intact HIV particles, has
240 also suggested structural differences in middle helix region that suggest flexibility at the helical
241 bundle core[13].
242
243

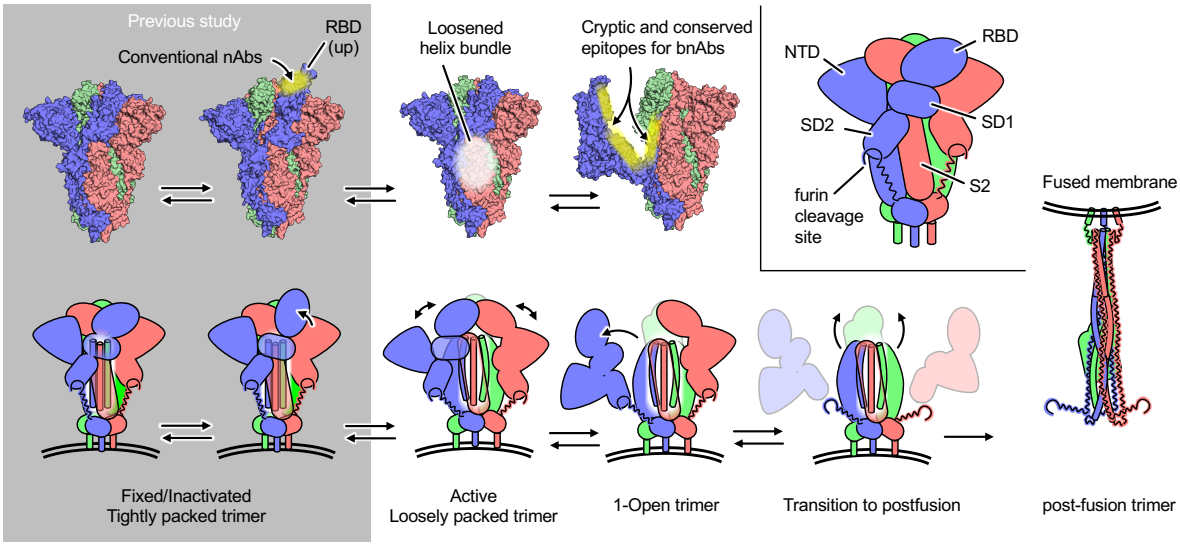

244

245 **Figure 4. Proposed model of spike structural changes for the membrane fusion.** (top right panel)
246 Schematic representation of the spike structure with the domain organization. The color of each protomer
247 corresponds to Fig. 2e. (top left to center) New cryptic sites of the S2 subunit exposed in open-trimer
248 conformations of the spike protein, potential targets for vaccine and antibodies/drugs. (bottom) Schematic

presentation of the proposed fusion mechanism. Fixed or recombinant spikes protein take a closed or Up RBD structure (gray box). On the active virus, spike proteins exist as a loosely packed trimer, with a partially opened S1 subunit. When the ACE2 binding promotes the S2 subdomain exposure, the S2 subunit irreversibly refolds to the postfusion state to fuse the viral envelope with the host cell membrane.

Implication on Fusion mechanism and Rational Vaccine and Antibody/Drug Design

Mutations of the spike protein are a major underlying cause for immune escape and reduction of vaccine efficiency. The development of broadly neutralizing antibodies (bnAbs) is important for preparedness for future pandemics. The recent review of Zhou et al. summarized three major non-RBD sites targeted for bnAbs, (1) fusion peptide, (2) SD1 (the S1 subdomain 1) and (3) the C-terminal stem helix[31]. Our cryo-ET map shows that the spike protein is flexible enough for these sites to be to some extent exposed in open-trimer structures, possibly generating bnAbs that exhibit neutralizing activity but with less potency. Either cocktails or bispecific forms of bnAbs, which can recognize different epitopes of single spike protein spontaneously, may improve the activity and tolerate mutations[31].

The development of long-term and broadly effective vaccines also requires new strategies to target highly conserved epitope regions[32,33]. Unlike RBD which is a hot spot for mutations, the S2 subunit shows higher conservation, wherein few mutations have emerged since the start of the pandemic. In fact, the fusion peptide (FP) and heptad repeat regions (HR1 and HR2) of the S2 subunit are more conserved within all coronaviruses including SARS-CoV-1 and Middle East respiratory syndrome coronavirus (MERS)-CoV[33]. This emphasizes the potential of developing broadly effective vaccines that may cover current and future coronavirus outbreaks. However, in current vaccine development strategies, the S2 subunit is considered as inaccessible, wherein proline mutations are applied to further stabilize the prefusion state. On the contrary, our Cryo-ET

273 study here suggests the dynamic nature of the spike protein where parts of the S2 subunit are
274 accessible (**Fig. 2c and Fig. 4**). As described above, bnAbs may exhibit less potent activity but
275 vaccine-induced bnAbs would overcome this limitation, while the stabilization of the S2 subunit
276 may be necessary. In fact, the development of a multivalent S2-based vaccine was recently shown
277 to provide a wide effect against beta, delta and omicron variants as well as pangolin coronavirus[32].

278 Besides the S2 subunit, the currently observed dynamics of the active SARS-CoV-2 virus
279 (**Fig. 4**) indicates the accessibility of the interface of S1 and S2 subunits. Note that these regions
280 are conserved across SARS-CoV-2 variants. Indeed, the HDX-MS experiment of the recombinant
281 spike protein also shows the increased accessibility of the two subdomains (SD1 and SD2) in the
282 S1 subunit[23]. Collectively, accounting for spike dynamics and cryptic epitope formation may
283 facilitate the development of broadly effective vaccines. For instance, a vaccine design based on
284 the spike protomer may better account for spike protein dynamics, exposing cryptic epitopes (**Fig.
285 4 and Fig. S6**). To explore monomer dynamics, Molecular Dynamics (MD) simulations of the
286 spike monomer of the Omicron BA.2 variant were performed. **Fig. S7** shows that a large range of
287 motions in the S1 subunit can be observed in the absence of the trimeric complex, exposing cryptic
288 pockets located at the interface of the S2 subunit, RBD, and the SD1 subdomain, which may induce
289 a broader spectrum of immune effect. Indeed, monoclonal antibodies (mAbs) targeting cryptic
290 epitopes, such as CR3022, P008-60, and sd1.040, can break up spike trimeric structure[34-36]. It is
291 worth mentioning that an early study has reported the feasibility of using a monomeric spike
292 protein of SARS-CoV-1 as a vaccine candidate[37].

293 Unexpectedly, the active dynamics of the spike protein structure, especially open-trimer
294 conformations, reveal benefits for fusion efficiency. A small percentage of open-trimer
295 conformations definitively expose the S2' cleavage site for TMPRSS2 and cathepsins. In this sense,

296 the spike protein possesses the inherent potential to allow the S1-S2 dissociation, inducing the
297 exposure of the S2' cleavage site. This process could be further facilitated by the ACE2 binding
298 (**Fig. 4**). In retrospect, the effect of the D614G mutation would be anticipated to lead to a larger
299 exposure.

300 The spike protein in active virus is highly dynamic with multiple levels of flexibility
301 including, membrane diffusibility, stalk region knee-like motion[17], RBD Down to Up transition[38]
302 and open-trimer formation[23]. In addition, it is highly susceptible to change in temperature, pH and
303 even glycosylation[9,39]. Structural analysis using inactivated viruses or recombinant proteins is
304 essential, however, the effect of mutations, chemical fixations, and trimerization tags shall be
305 considered. Hence, it is crucial to study viral proteins in their native, active state. Cryo-ET at BSL3
306 facility is expected to be an indispensable method to tackle current and future pandemics.
307

308 **Methods**

309 **Virus preparation**

310 An ancestral SARS-CoV-2 strain, WK-521 (GISAID: EPI_ISL_408667), was kindly
311 provided by Dr. Shimojima (National Institute of Infectious Diseases, Japan). The viral stock was
312 prepared by the inoculation to Vero E6 cells constantly expressing human TMPRSS2 (Vero
313 E6/TMPRSS2)[40]. At 2 days post-infection (dpi), the culturing supernatant was centrifuged at 440
314 × *g* for 2 min to remove the cell debris and stored at −80 °C as a virus stock. The titer of the stock
315 was determined by plaque assay as previously described[41]. In brief, Vero E6/TMPRSS2 cells were
316 inoculated with serial dilutions of virus stock for 1 h at 37 °C. The cells were overlaid with
317 Dulbecco's Modified Eagle Medium (Nissui) containing 2% FBS and 0.5% Bacto Agar (Becton
318 Dickinson). At 2 dpi, cells were fixed with 3.7% formaldehyde in phosphate-buffered saline (PBS)
319 and stained with 1% crystal violet.

320 For the preparation of the cryo-ET sample, Vero E6/TMPRSS2 cells in a 6 well plate were
321 inoculated with the virus at a multiplicity of infection (MOI) of 10 and incubated for 1 h at 37 °C.
322 The media was then replaced with 400 μL of fresh Opti-MEM (Thermo Fisher Scientific). At 18 h
323 post-infection, culture supernatant was collected and clarified with 0.45 μm filtration. The sample
324 was kept at 37 °C and used immediately for grid preparation.

325

326 **Data collection**

327 For cryo-ET, 2 μL of sample was applied on each side of a freshly glow-discharged
328 QUANTIFOIL R 1.2/1.3 Cu 200-mesh grid (Quantifoil Micro Tools). The grid was blotted at once
329 for 15 s from the back side and plunged into liquid ethane using EM GP2 (Leica Microsystems) at
330 18 °C and 90% humidity chamber setting. The micrograph images were collected on a Krios G4

(Thermo Fisher Scientific) operating at a voltage of 300 kV with an energy filter Selectris (slit width 10 eV) and a direct electron detector Falcon 4. Each micrograph was collected at a nominal magnification of 64,000× (pixel size of 1.88Å) with an exposure time of 0.73 s (dose of 1.5 e/Å^2) at a underfocus of 0.2 μm using a Volta phase plate (VPP). Tilt-series data collection was performed with a dose-symmetric scheme tilting by 1° steps from −60° to 60° using Tomography software (Thermo Fisher Scientific), **Table S2**.

Cryo-Electron Tomography Data Processing.

42 micrographs were processed using the IMOD package[42]. Patch tracking was used to align tilt images. Ctfplotter was used to estimate defocus, phase shift, and astigmatism within the context of the contrast transfer function[43]. Tomograms were binned 4x and reconstructed with weighted back projection with a voxel size of 7.536 Å. SIRT-like filtered tomograms were generated for visualization and particle picking. Reconstructed tomograms were also imported and filtered in EMAN2[44]. Virus particles were manually segmented in EMAN2 and used for isosurface visualization in Chimera-X software[45]. The two longest diameters of viruses and the thickness of ice layer were calculated using 3dmod.

291 spike proteins, from 46 virions, were manually picked from the 4-fold binned SIRT tomograms, including pre (247 particles) and postfusion (44 particles) states. The sub-tomogram averaging of the prefusion state were processed in Relion 4.0[26]. The reference-free alignment was performed, where the initial map was generated from the binned subtomograms and used subsequently for other refinements. After obtaining an adequately representative map, the C3 symmetry was invoked. A series of refinements were performed starting from 4x binning to 2x to unbinned. Finally, several cycles of the 3D refinement were performed at a voxel size of 1.884 Å

354 on unbinned subtomograms. After the 3D refinement, the CTF was corrected using ctffind-4.1.14[46]
355 and 2D images alignment was improved in each cycle. The cycles were repeated until no further
356 improvement in resolution was observed. The final average map of the C3 symmetry was estimated
357 to have 14.3 Å resolution at FSC = 0.143 cutoff in RELION4.0. To understand the effect of
358 symmetries, a final cycle of refinement was performed with C1 symmetry, providing a 17.0 Å
359 resolution map. The models of the spike protein, PDB 6ZGE and 7M0J, were rigid fitted in the C3
360 map using ChimeraX[45]. PyMOL software was used for visualizing the structures [47].
361
362
363
364

References

1 Hu, B., Guo, H., Zhou, P. & Shi, Z. L. Characteristics of SARS-CoV-2 and COVID-19. *Nat Rev Microbiol* **19**, 141-154 (2021). https://doi.org:10.1038/s41579-020-00459-7

2 Cao, Y. *et al.* Omicron escapes the majority of existing SARS-CoV-2 neutralizing antibodies. *Nature* **602**, 657-663 (2022). https://doi.org:10.1038/s41586-021-04385-3

3 Tamura, T. *et al.* Virological characteristics of the SARS-CoV-2 XBB variant derived from recombination of two Omicron subvariants. *Nat Commun* **14**, 2800 (2023). https://doi.org:10.1038/s41467-023-38435-3

4 Saville, J. W., Berezuk, A. M., Srivastava, S. S. & Subramaniam, S. Three-Dimensional Visualization of Viral Structure, Entry, and Replication Underlying the Spread of SARS-CoV-2. *Chem Rev* **122**, 14066-14084 (2022). https://doi.org:10.1021/acs.chemrev.1c01062

5 Wang, Q. *et al.* Structural and Functional Basis of SARS-CoV-2 Entry by Using Human ACE2. *Cell* **181**, 894-904 e899 (2020). https://doi.org:10.1016/j.cell.2020.03.045

6 Cai, Y. *et al.* Distinct conformational states of SARS-CoV-2 spike protein. *Science* **369**, 1586-1592 (2020). https://doi.org:10.1126/science.abd4251

7 Xu, C., Han, W. & Cong, Y. Cryo-EM and cryo-ET of the spike, virion, and antibody neutralization of SARS-CoV-2 and VOCs. *Curr Opin Struct Biol* **82**, 102664 (2023). https://doi.org:10.1016/j.sbi.2023.102664

8 Wrapp, D. *et al.* Cryo-EM structure of the 2019-nCoV spike in the prefusion conformation. *Science* **367**, 1260-1263 (2020). https://doi.org:10.1126/science.abb2507

9 Zhou, T. *et al.* Cryo-EM Structures of SARS-CoV-2 Spike without and with ACE2 Reveal a pH-Dependent Switch to Mediate Endosomal Positioning of Receptor-Binding Domains. *Cell Host Microbe* **28**, 867-879 e865 (2020). https://doi.org:10.1016/j.chom.2020.11.004

10 Wrobel, A. G. *et al.* SARS-CoV-2 and bat RaTG13 spike glycoprotein structures inform on virus evolution and furin-cleavage effects. *Nat Struct Mol Biol* **27**, 763-767 (2020). https://doi.org:10.1038/s41594-020-0468-7

11 Fan, X., Cao, D., Kong, L. & Zhang, X. Cryo-EM analysis of the post-fusion structure of the SARS-CoV spike glycoprotein. *Nat Commun* **11**, 3618 (2020). https://doi.org:10.1038/s41467-020-17371-6

12 Saito, A. *et al.* Virological characteristics of the SARS-CoV-2 Omicron BA.2.75 variant. *Cell Host Microbe* **30**, 1540-1555 e1515 (2022). https://doi.org:10.1016/j.chom.2022.10.003

13 Mangala Prasad, V. *et al.* Cryo-ET of Env on intact HIV virions reveals structural variation and positioning on the Gag lattice. *Cell* **185**, 641-653 e617 (2022). https://doi.org:10.1016/j.cell.2022.01.013

14 Calder, L. J., Calcraft, T., Hussain, S., Harvey, R. & Rosenthal, P. B. Electron cryotomography of SARS-CoV-2 virions reveals cylinder-shaped particles with a double layer RNP assembly. *Commun Biol* **5**, 1210 (2022). https://doi.org:10.1038/s42003-022-04183-1

15 Song, Y. *et al.* In situ architecture and membrane fusion of SARS-CoV-2 Delta variant. *Proc Natl Acad Sci U S A* **120**, e2213332120 (2023). https://doi.org:10.1073/pnas.2213332120

16 Yao, H. *et al.* Molecular Architecture of the SARS-CoV-2 Virus. *Cell* **183**, 730-738 e713 (2020). https://doi.org:10.1016/j.cell.2020.09.018

17 Turonova, B. *et al.* In situ structural analysis of SARS-CoV-2 spike reveals flexibility mediated by three hinges. *Science* **370**, 203-208 (2020). https://doi.org:10.1126/science.abd5223

18 Mendonca, L. *et al.* Correlative multi-scale cryo-imaging unveils SARS-CoV-2 assembly and egress. *Nat Commun* **12**, 4629 (2021). https://doi.org:10.1038/s41467-021-24887-y

19 Zimmermann, L. & Chlanda, P. Cryo-electron tomography of viral infection - from applications to biosafety. *Curr Opin Virol* **61**, 101338 (2023). https://doi.org:10.1016/j.coviro.2023.101338

20 Hsieh, C. L. *et al.* Structure-based design of prefusion-stabilized SARS-CoV-2 spikes. *Science* **369**, 1501-1505 (2020). https://doi.org:10.1126/science.abd0826

21 Juraszek, J. *et al.* Stabilizing the closed SARS-CoV-2 spike trimer. *Nat Commun* **12**, 244 (2021). https://doi.org:10.1038/s41467-020-20321-x

22 Claireaux, M. *et al.* A public antibody class recognizes an S2 epitope exposed on open conformations of SARS-CoV-2 spike. *Nat Commun* **13**, 4539 (2022). https://doi.org:10.1038/s41467-022-32232-0

23 Costello, S. M. *et al.* The SARS-CoV-2 spike reversibly samples an open-trimer conformation exposing novel epitopes. *Nat Struct Mol Biol* **29**, 229-238 (2022). https://doi.org:10.1038/s41594-022-00735-5

24 Ichikawa, T. *et al.* Chemical fixation creates nanoscale clusters on the cell surface by aggregating membrane proteins. *Commun Biol* **5**, 487 (2022). https://doi.org:10.1038/s42003-022-03437-2

25 Silva, R. P. *et al.* Identification of a conserved S2 epitope present on spike proteins from all highly pathogenic coronaviruses. *Elife* **12** (2023). https://doi.org:10.7554/eLife.83710

26 Zivanov, J. *et al.* A Bayesian approach to single-particle electron cryo-tomography in RELION-4.0. *Elife* **11** (2022). https://doi.org:10.7554/eLife.83724

27 Bangaru, S. *et al.* Structural analysis of full-length SARS-CoV-2 spike protein from an advanced vaccine candidate. *Science* **370**, 1089-1094 (2020). https://doi.org:10.1126/science.abe1502

28 Gobeil, S. M. *et al.* Effect of natural mutations of SARS-CoV-2 on spike structure, conformation, and antigenicity. *Science* **373** (2021). https://doi.org:10.1126/science.abi6226

29 Henderson, R. *et al.* Controlling the SARS-CoV-2 spike glycoprotein conformation. *Nat Struct Mol Biol* **27**, 925-933 (2020). https://doi.org:10.1038/s41594-020-0479-4

30 Dokainish, H. M. & Sugita, Y. Structural effects of spike protein D614G mutation in SARS-CoV-2. *Biophys J* **122**, 2910-2920 (2023). https://doi.org:10.1016/j.bpj.2022.11.025

31 Zhou, D., Ren, J., Fry, E. E. & Stuart, D. I. Broadly neutralizing antibodies against COVID-19. *Curr Opin Virol* **61**, 101332 (2023). https://doi.org:10.1016/j.coviro.2023.101332

32 Halfmann, P. J. *et al.* Multivalent S2-based vaccines provide broad protection against SARS-CoV-2 variants of concern and pangolin coronaviruses. *EBioMedicine* **86**, 104341 (2022). https://doi.org:10.1016/j.ebiom.2022.104341

33 Olukitibi, T. A. *et al.* Significance of Conserved Regions in Coronavirus Spike Protein for Developing a Novel Vaccine against SARS-CoV-2 Infection. *Vaccines (Basel)* **11** (2023). https://doi.org:10.3390/vaccines11030545

34 Huo, J. *et al.* Neutralization of SARS-CoV-2 by Destruction of the Prefusion Spike. *Cell Host Microbe* **28**, 445-454 e446 (2020). https://doi.org:10.1016/j.chom.2020.06.010

35 Seow, J. *et al.* A neutralizing epitope on the SD1 domain of SARS-CoV-2 spike targeted following infection and vaccination. *Cell Rep* **40**, 111276 (2022). https://doi.org:10.1016/j.celrep.2022.111276

36 Bianchini, F. *et al.* Human neutralizing antibodies to cold linear epitopes and subdomain 1 of the SARS-CoV-2 spike glycoprotein. *Sci Immunol* **8**, eade0958 (2023). https://doi.org:DOI: 10.1126/sciimmunol.ade0958

37 Li, J., Ulitzky, L., Silberstein, E., Taylor, D. R. & Viscidi, R. Immunogenicity and protection efficacy of monomeric and trimeric recombinant SARS coronavirus spike protein subunit vaccine candidates. *Viral Immunol* **26**, 126-132 (2013). https://doi.org:10.1089/vim.2012.0076

38 Dokainish, H. M. *et al.* The inherent flexibility of receptor binding domains in SARS-CoV-2 spike protein. *Elife* **11** (2022). https://doi.org:10.7554/eLife.75720

39 Olia, A. S. *et al.* SARS-CoV-2 S2P spike ages through distinct states with altered immunogenicity. *J Biol Chem* **297**, 101127 (2021). https://doi.org:https://doi.org/10.1016/j.jbc.2021.101127

40 Sasaki, M. *et al.* SARS-CoV-2 Bearing a Mutation at the S1/S2 Cleavage Site Exhibits Attenuated Virulence and Confers Protective Immunity. *mBio* **12**, e0141521 (2021). https://doi.org:10.1128/mBio.01415-21

41 Sasaki, M. *et al.* S-217622, a SARS-CoV-2 main protease inhibitor, decreases viral load and ameliorates COVID-19 severity in hamsters. *Sci Transl Med* **15**, eabq4064 (2023). https://doi.org:10.1126/scitranslmed.abq4064

42 Kremer, J. R., Mastronarde, D. N. & McIntosh, J. R. Computer visualization of three-dimensional image data using IMOD. *J Struct Biol* **116**, 71-76 (1996). https://doi.org:10.1006/jsbi.1996.0013

43 Xiong, Q., Morphew, M. K., Schwartz, C. L., Hoenger, A. H. & Mastronarde, D. N. CTF determination and correction for low dose tomographic tilt series. *J Struct Biol* **168**, 378-387 (2009). https://doi.org:10.1016/j.jsb.2009.08.016

44 Tang, G. *et al.* EMAN2: an extensible image processing suite for electron microscopy. *J Struct Biol* **157**, 38-46 (2007). https://doi.org:10.1016/j.jsb.2006.05.009

45 Pettersen, E. F. *et al.* UCSF ChimeraX: Structure visualization for researchers, educators, and developers. *Protein Sci* **30**, 70-82 (2021). https://doi.org:10.1002/pro.3943

46 Rohou, A. & Grigorieff, N. CTFFIND4: Fast and accurate defocus estimation from electron micrographs. *J Struct Biol* **192**, 216-221 (2015). https://doi.org:10.1016/j.jsb.2015.08.008

47 Schrodinger, LLC. *The PyMOL Molecular Graphics System, Version 2.4*.

Acknowledgements

We thank Hiroshi Kida, Tatsuya Zenko, Atsushi Furukawa, Takashi Tadokoro, Robert Parsons, Peijun Zhang, Fabian Eisenstein, Radostin Danev, Makoto Takeda for their support and discussions. We also thank members of Facilities Division of Hokkaido University and Thermofisher Scientific (Yoshihiro Tomatsu, Kazuhiro Aoyama, Yu Yong) for their technical assistance. This work was supported in part by the Japan Agency for Medical Research and Development (AMED) [JP17am0101093 (K.M.), JP20ae0101047 (K.M.), JP21fk0108463 (K.M.), JP22ama121037 (K.M.), JP223fa627005 (K.M, K.T, M.S, Y.O, and H.S.), JP23ama121001 (T.S.)], Hokkaido University Biosurface project (K.M.), Japan Science and Technology Agency (JST) CREST grant number JPMJCR20H8 (H.F), JSPS Strategic Young Researcher Overseas Visits Program for Accelerating Brain Circulation (K.M.), the Scientific Research on Innovative Areas and International Group from the MEXT/JSPS KAKENHI [JP20H05873 (K.M)], 23HA2010 by Ministry of Health, Labour and Welfare (MHLW) (H.S.), and Takeda Science Foundation (K.M.). This research used computational resources of the supercomputer Fugaku (hp230052 and hp220087) provided by the RIKEN Center for Computational Science (the evaluation environment in the trial phase).

Author contributions

H.F., H.M.D., and K.M. designed the study; H.F., S.K., Y.S., H.S. and K.M. set up BSL3 Cryo-EM facility; J.T.H. and D.I.S. assisted to set up and consult about BSL3 Cryo-EM facility; H.F., K.T, M.S., Y.O., and H.S. prepared virus solution; H.F., S.K., K.T., Y.A., and H.S. performed Cryo-ET data collection; H.M.D. performed Cryo-ET analysis; S.K., J.T.H., and K.M. advised

502 Cryo-ET analysis. A.S. T.S., and K.M. designed and prepared unique device of sample transfer for
503 Cryo-ET; H.M.D., H.F., and K.M. wrote the manuscript.
504
505 **Competing interests**
506 The authors declare no competing interests.
507
508 **Data availability**
509 All other data are available from the corresponding author upon request. Methods
510 describing structure determination are included in Supplementary Methods.
511

Snapshots from Cryo-ET of active SARS-CoV-2 virions

Hideo Fukuhara[1,2,#], Hisham M. Dokainish[2,#,*], Shunsuke Kita[2], Koshiro Tabata[3,4], Akira Takasu[5], Juha T. Huiskonen[6], Yuki Anraku[2], Toshiya Senda[5,7,8], David I. Stuart[9], Michihito Sasaki[3], Yasuko Orba[3], Yasuhiko Suzuki[4,10,*], Hirofumi Sawa[3,4,12,*] & Katsumi Maenaka[1,2,4,13,14,15,*].

Supplementary material

(Figure S1 to S7 and Table S1, S2)

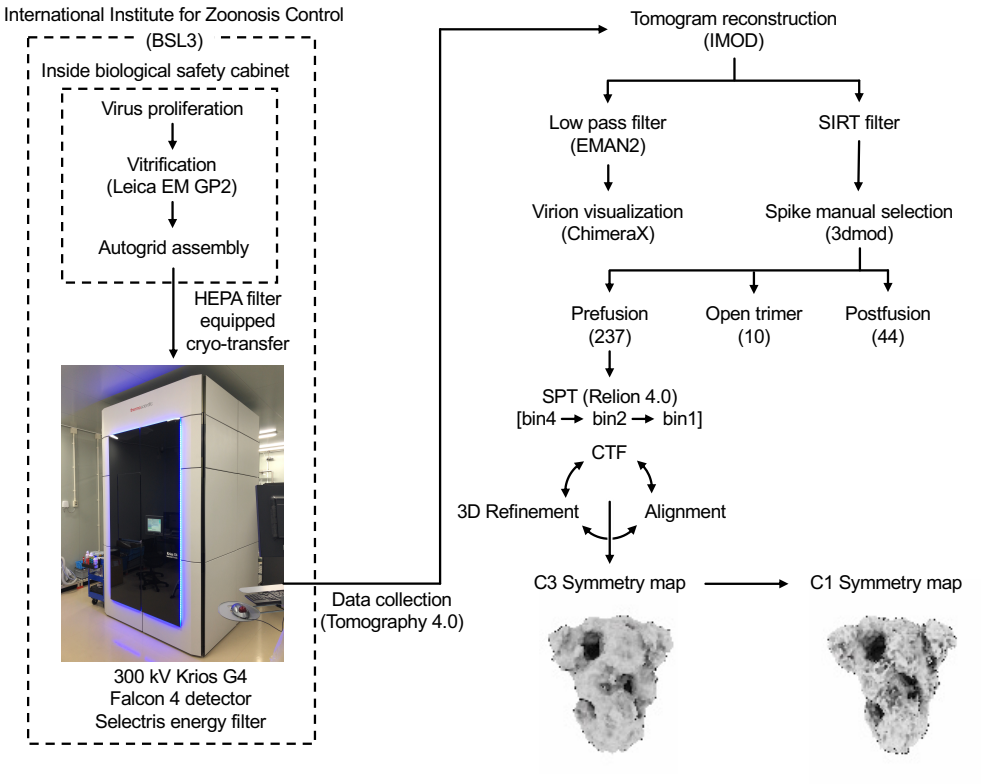

Figure S1. BSL3 Cryo-EM facility at Hokkaido University and Cryo-ET analysis scheme.

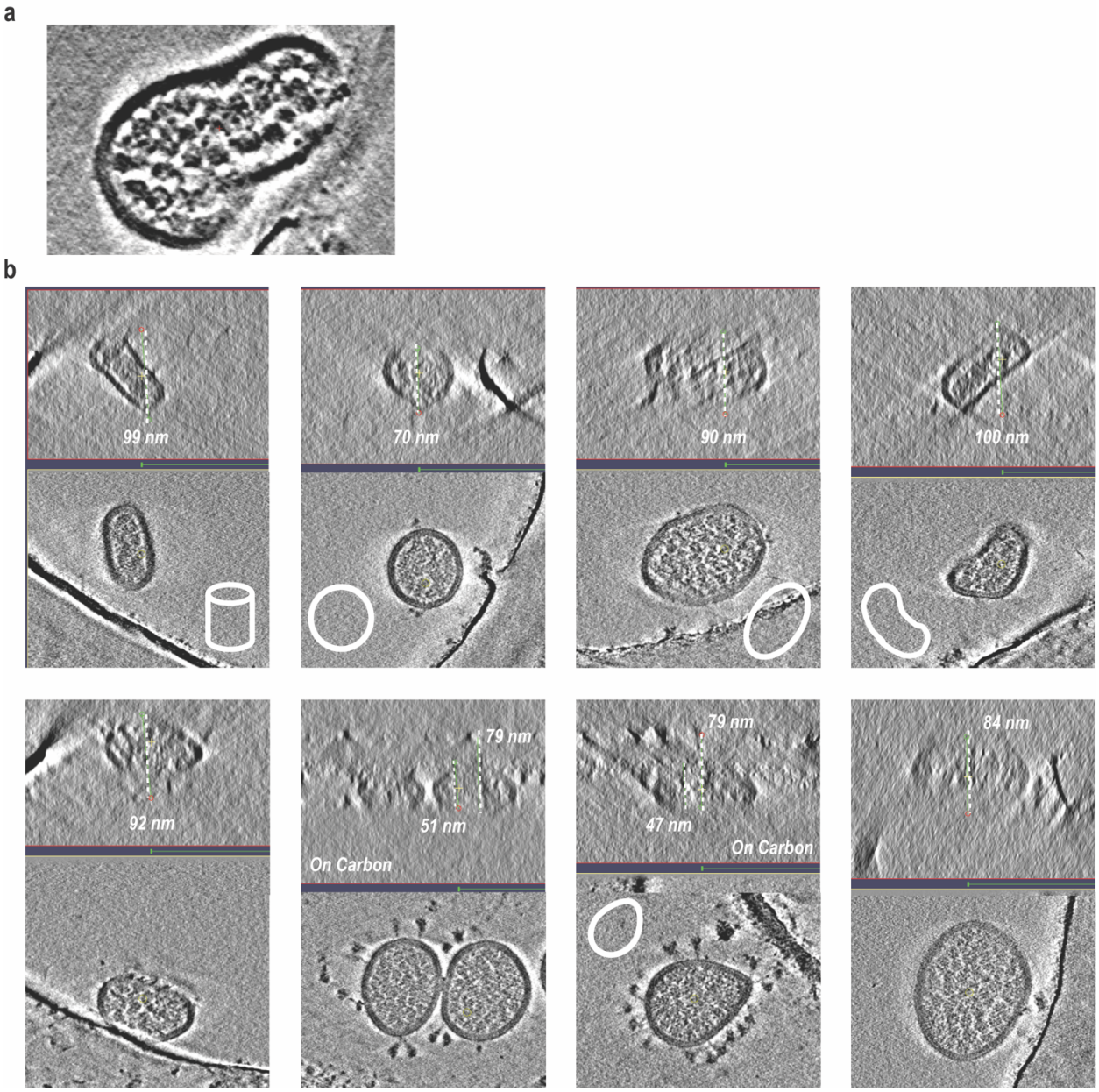

Figure S2. Particle morphology and ice thickness. a) Tomogram slice of two virion particles undergoing fusion process. b) Side and central sections through the cryo-ET tomogram of the ancestral virions particles with different morphology. Ice thickness is highlighted by dotted line and reported in nm.

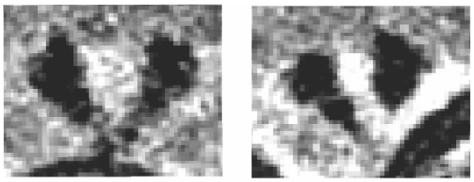

Spikes with shared Stem

Figure S3. 2D slice of full spike protein structures with shared stems.

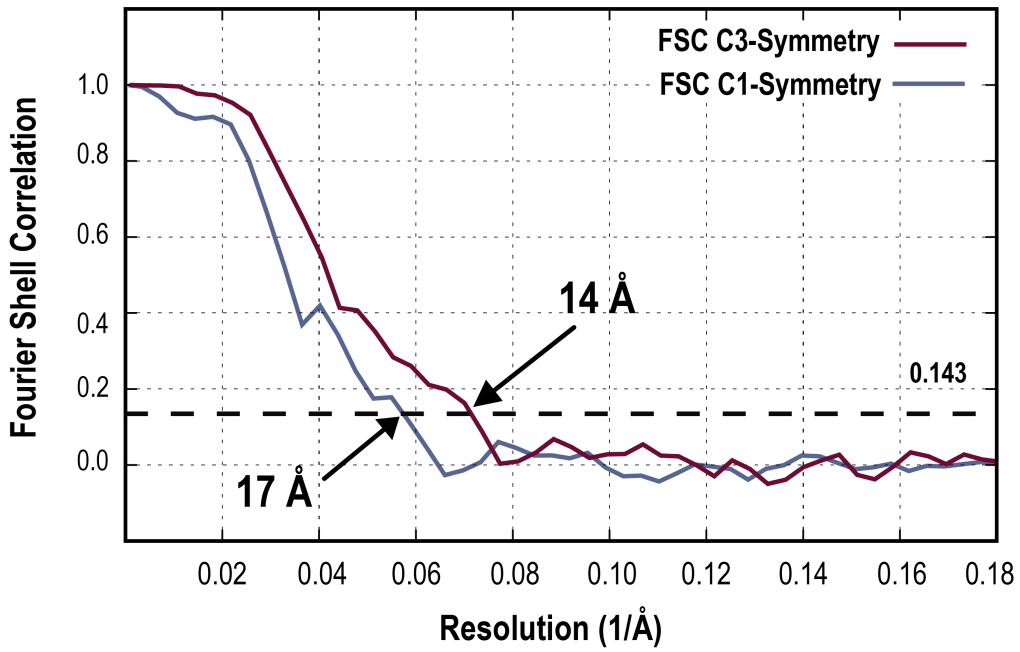

Figure S4. Gold-standard Fourier shell correlation (FSC) curves for C3 and C1 symmetrized maps. Dotted line indicates the 0.143 FSC cutoff.

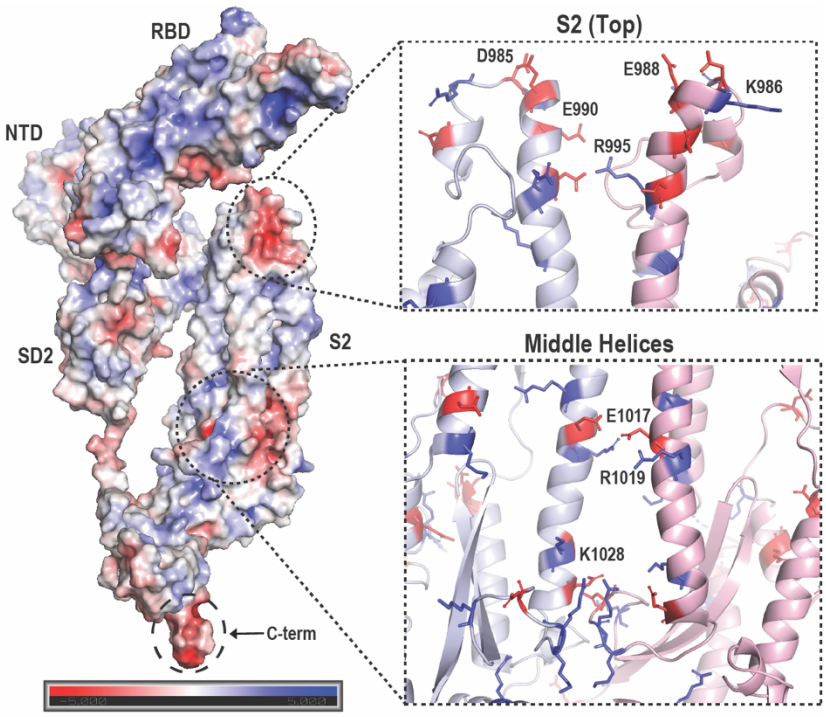

Figure S5. Charge distribution in Spike protomer. Electrostatic surface representation of the spike protein protomer from the high resolution structure (PDB 6ZGE)[1]. Highly charged regions are highlighted with dotted lines. Ribbon representation of the middle and top regions of S2 interface from two protomers with highlighted charged residues. Blue and red sticks represent positively and negatively charged amino acids, respectively.

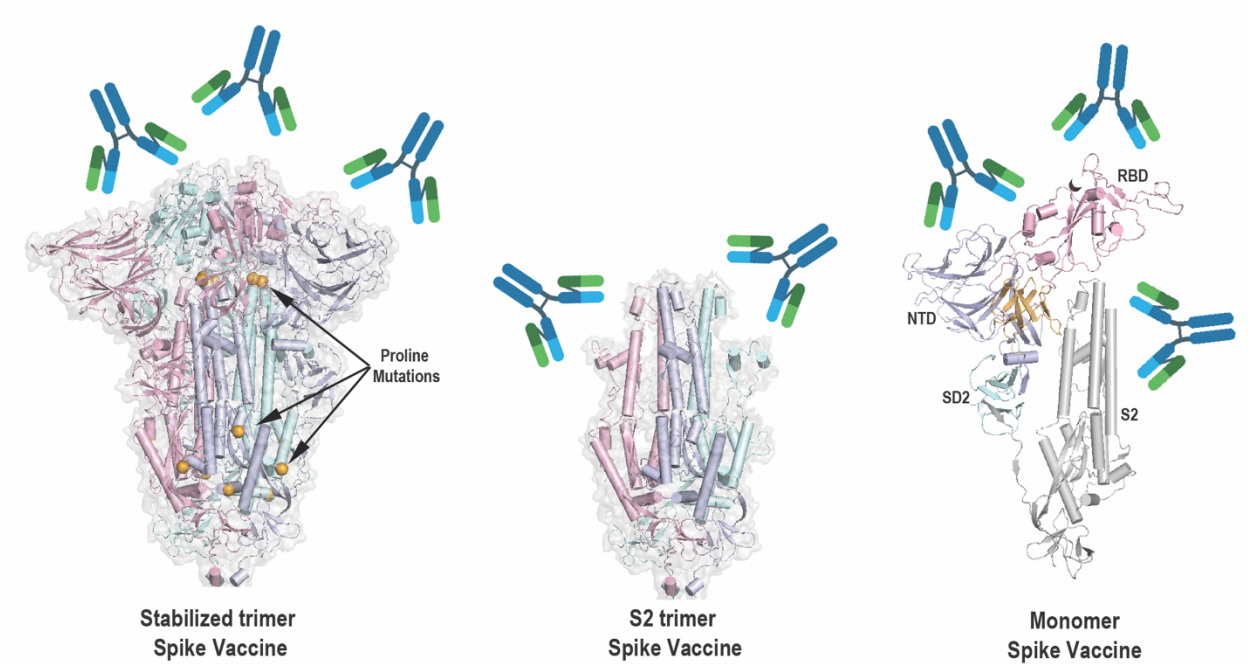

Figure S6. SARS-CoV2 vaccine design approaches. Left: The cartoon representation of second generation of SARS-CoV-2 Vaccines that include 6 proline mutations (shown as orange spheres), inducing mainly RBD and NTD neutralizing Abs. Middle: S2-based vaccine approach that allow for targeting the S2 region. Right: Monomer-based vaccine approach to account for protein dynamic and target both S1 and S2 regions. Antibodies (blue and green) are schematically shown in all figures.

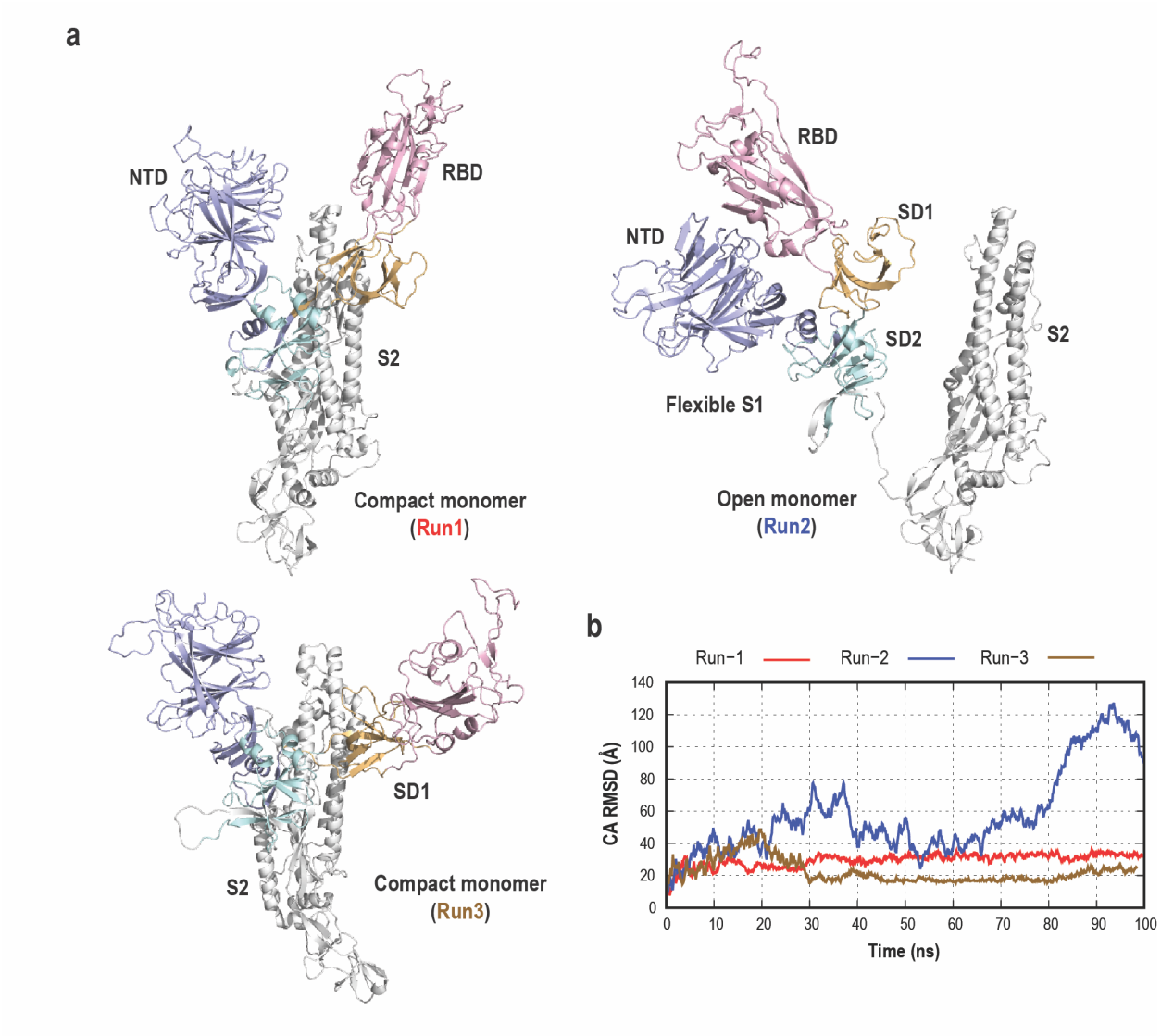

Figure S7. Conformational flexibility in the spike protein isolated monomer. a) Cartoon representation of different conformations of the head region of spike protomer obtained from three independent MD simulations. Two simulations form compact monomers conformations, while one simulation shows the opening of the S1 subunit (open monomer). b) Root mean square deviations (RMSD) of the Cα atoms upon fitting S2 region. All simulations show large deviation from a starting structure due to the motion of the S1 subunit.

Table S1. All particles diameter measurements (L1 and L2) in nm.

Ellipsoidal		Spherical		Oval		Bean-shape		Cylindrical	
L1	*L2*	*L1*	*L2*	*L1*	*L2*	*L1*	*L2*	*L1*	*L2*
101	88	90	81	122	89	86	51	105	61
125	100	105	104	107	101	109	65	94	49
125	119	107	102	97	83	119	66	91	50
150	125	102	93	71	76	89	79	92	73
147	88	105	101			94	55	83	52
99	83	87	86			103.0	75.0		
139	102	88	84						
108	86	108	102						
109	95	104	98						
97	81	85	82						
102	74	109	105						
103	87	83	78						
		94	94						
		106	94						
		142	138						
		90	86						
		98	98						
		94	91						
		86	82						

Table S2. Cryo-ET data acquisition and reconstruction statistics.

Data Collection		
Microscope	Titan Krios G4	
Magnification	64,000	
Voltage (kV)	300	
Detector	Falcon 4	
Energy filter	Selectris	
Pixel size (Å)	1.884	
Tilt Schemes	Dose-symmetric scheme	
Tilt angle increment (degree)	1	
Tilt angle range	-60 to +60	
Number of tilt Series	42	
Number of virions	46	
Defocus	0.2 using Volta Phase Plate	
Software	Tomography 4	
Total dose (e/Å^2)	181.5	
Reconstruction		
Software	IMOD, Relion	
Dataset	Prefusion spike	
Number of spikes	237	
Symmetry	C3	C1
Final resolution (Å)	14.3	17.0
Gold-standard	yes	yes
FSC threshold	0.143	0.143
Final pixelsize (Å)	1.884	1.884

Supplementary Method:

MD simulations of Spike monomer.

The monomeric spike protein model was based on the Omicron BA.2 Cryo-EM structure (PDB 7UB0)[2]. CHARMM-GUI was used to add missing residues, ions, water molecules for preparing final simulation model[3]. Glycan and disulfide bonds were added in a similar fashion to previous study[4]. Considering the potential large motion in monomer spike protein, a large box size was used with total number of atoms of 742586. All simulations were performed using GENESIS 2.0 Beta MD software on Fugaku supercomputer[5,6]. Three independent simulations for 100 ns each was performed using CHARMM 36M force field for protein residues and CHARMM TIP3P for ions and water molecules[7,8]. VMD software was used for trajectory visualization [9].

References

1 Wrobel, A. G. *et al.* SARS-CoV-2 and bat RaTG13 spike glycoprotein structures inform on virus evolution and furin-cleavage effects. *Nat Struct Mol Biol* **27**, 763-767 (2020). https://doi.org:10.1038/s41594-020-0468-7

2 Stalls, V. *et al.* Cryo-EM structures of SARS-CoV-2 Omicron BA.2 spike. *Cell Rep* **39**, 111009 (2022). https://doi.org:10.1016/j.celrep.2022.111009

3 Lee, J. *et al.* CHARMM-GUI Input Generator for NAMD, GROMACS, AMBER, OpenMM, and CHARMM/OpenMM Simulations Using the CHARMM36 Additive Force Field. *J. Chem. Theory Comput.* **12**, 405-413 (2016). https://doi.org:10.1021/acs.jctc.5b00935

4 Dokainish, H. M. *et al.* The inherent flexibility of receptor binding domains in SARS-CoV-2 spike protein. *Elife* **11** (2022). https://doi.org:10.7554/eLife.75720

5 Kobayashi, C. *et al.* GENESIS 1.1: A hybrid-parallel molecular dynamics simulator with enhanced sampling algorithms on multiple computational platforms. *J Comput Chem* **38**, 2193-2206 (2017). https://doi.org:10.1002/jcc.24874

6 Jung, J. *et al.* New parallel computing algorithm of molecular dynamics for extremely huge scale biological systems. *J Comput Chem* **42**, 231-241 (2021). https://doi.org:10.1002/jcc.26450

7 Huang, J. *et al.* CHARMM36m: an improved force field for folded and intrinsically disordered proteins. *Nat. Methods* **14**, 71-73 (2017). https://doi.org:10.1038/nmeth.4067

8 Guvench, O. *et al.* CHARMM additive all-atom force field for carbohydrate derivatives and its utility in polysaccharide and carbohydrate-protein modeling. *J. Chem. Theory Comput.* **7**, 3162-3180 (2011). https://doi.org:10.1021/ct200328p

9 Humphrey, W., Dalke, A. & Schulten, K. VMD: visual molecular dynamics. *J Mol Graph* **14**, 33-38, 27-38 (1996). https://doi.org:10.1016/0263-7855(96)00018-5